ARTICLE

Check for updates

Coastal permafrost was massively eroded during the Bølling-Allerød warm period

Alessio Nogarotto [1,2✉], Riko Noormets[3], Teena Chauhan[4], Gesine Mollenhauer [5,6], Jens Hefter [5], Hendrik Grotheer [5], Simon T. Belt[7], Florence Colleoni[8], Francesco Muschitiello[9], Lucilla Capotondi [10], Claudio Pellegrini[10] & Tommaso Tesi[2]

The Bølling-Allerød interstadial (14,700–12,900 years before present), during the last deglaciation, was characterized by rapid warming and sea level rise. Yet, the response of the Arctic terrestrial cryosphere during this abrupt climate change remains thus far elusive. Here we present a multi-proxy analysis of a sediment record from the northern Svalbard continental margin, an area strongly influenced by sea ice export from the Arctic, to elucidate sea level - permafrost erosion connections. We show that permafrost-derived material rich in biospheric carbon became the dominant source of sediments at the onset of the Bølling-Allerød, despite the lack of direct connections with permafrost deposits. Our results suggest that the abrupt temperature and sea level rise triggered massive erosion of coastal ice-rich Yedoma permafrost, possibly from Siberian and Alaskan coasts, followed by long-range sea ice transport towards the Fram Strait and the Arctic Ocean gateway. Overall, we show how coastal permafrost is susceptible to large-scale remobilization in a scenario of rapid climate variability.

[1] Department of Environmental Sciences, Informatics and Statistics, Ca' Foscari University of Venice, 30172 Venezia, Italy. [2] Institute of Polar Sciences, National Research Council, 40129 Bologna, Italy. [3] Department of Arctic Geology, University Centre in Svalbard, PO box 156 Longyearbyen N-9171, Norway. [4] Department of Earth Science, University of Bergen, 5007 Bergen, Norway. [5] Alfred Wegener Institute, Helmholtz Centre for Polar and Marine Research, Marine Geochemistry, D-27570 Bremerhaven, Germany. [6] Department of Geosciences and MARUM Centre for Marine Environmental Sciences, University Bremen, D-28334 Bremen, Germany. [7] Biogeochemistry Research Centre, School of Geography, Earth and Environmental Sciences, University of Plymouth, Plymouth, Devon PL4 8AA, UK. [8] National Institute for Oceanography and Applied Geophysics, 34010 Sgonico (TS), Italy. [9] Department of Geography, University of Cambridge, Cambridge CB2 3EN, UK. [10] Institute of Marine Sciences, National Research Council, 40129 Bologna, Italy. ✉email: alessio.nogarotto@cnr.it

The last deglaciation (ca. 21-11 kiloyears before 1950 AD, hereafter reported as kyr BP) represents the transition from the Last Glacial Maximum (LGM) to the current Holocene interglacial. The general reorganization of global climate during this period affected atmospheric and oceanic temperature, sea level and biogeochemical cycles[1,2], particularly in the polar regions[3]. This transition is characterised by a series of abrupt climate changes, including the Bølling-Allerød interstadial (B-A; ca. 14.7-12.9 kyr BP[4]), the onset of which coincided with a period of enhanced sea level rise known as Meltwater Pulse 1 A (MWP-1A; ca. 14.7-14.3 kyr BP[5,6]). The B-A period is also characterised by a rapid warming of the North Atlantic region[7,8], and there is now a consensus that this climate transition was triggered by significant strengthening of the Atlantic Meridional Overturning Circulation (AMOC)[8–10]. During MWP-1A, sea level rose by approximately 18 m in less than 500 years (~4 cm yr^{-1}) as a result of the retreat of the Laurentide and Eurasian Ice Sheets (LIS and EIS) as well as the Antarctic Ice Sheet[5,6,11].

During the B-A, the northern hemisphere climate experienced important modifications that share similarities with the anticipated Polar Amplification[12–14]. Indeed, the destabilization of key elements of the cryosphere such as permafrost deposits and ice sheets is considered a threat to Earth's future climate because of their potential to further increase the concentrations of atmospheric Green House Gases (GHGs) and sea level rise[15–18], respectively. Thus, the study of past abrupt warming events offers the opportunity to understand the behaviour of permafrost in a scenario of rapid cryosphere retreat, as well as place the modern anthropogenically-induced permafrost-climate feedbacks into a broader context of natural centennial-scale climate variability.

Recent estimates indicate that the vast majority of carbon in permafrost regions during the LGM was found in loess and ice-rich deposits, while in modern times, considering the same areal extent, peatlands have become the dominant reservoir for organic carbon (OC)[19]. Overall, this indicates that a complete reorganization of OC reservoirs in Circumpolar Arctic soils must have taken place at some point during the last 20 kyr.

Between Marine Isotopic Stage (MIS) 5 and MIS 2 (ca. 120-18 kyr BP), the large sea level drop and the subsequent exposure of large portions of the Laptev Sea, East Siberian Sea and Chukchi Sea continental shelves caused the expansion of Ice Complex deposits[20–22], also referred to as Yedoma deposits, formed by fine-grained material with high amounts of OC and ice (up to 5% and 80%, respectively[23]). Today, the Yedoma domain represents approximately one third of the total OC stored in the Circumpolar Arctic permafrost region (327–466 Pg C), with Yedoma deposits accounting for 83-129 Pg C[17,24]. During the last glacial period, Yedoma deposits were a relatively large carbon pool, mainly because of the exposed land on Circum-Arctic shelves, with recent estimates indicating a potential carbon stock of 657 ± 97 Pg[24], suggesting that a significant portion of the permafrost OC loss, within the reorganization of OC reservoirs happened during the last 20 kyr, likely involved these deposits. In fact, previous modelling studies and records from coral reefs[25,26] also highlighted the potential contribution of Yedoma destabilization to deglacial atmospheric CO_2 increase.

In contrast, a recent study has suggested that Yedoma deposits remained relatively unaltered during the last deglaciation, with negligible changes to their extension and storage capabilities[19]. However, during post-glacial sea level rise, when the continental shelves were flooded, Yedoma deposits possibly became vulnerable to mechanical erosion and thermal degradation[24,27,28]. In any case, a survey of the recent literature clearly reveals how the exact processes and feedbacks regarding Yedoma permafrost erosion during the last deglaciation are still a matter of debate,
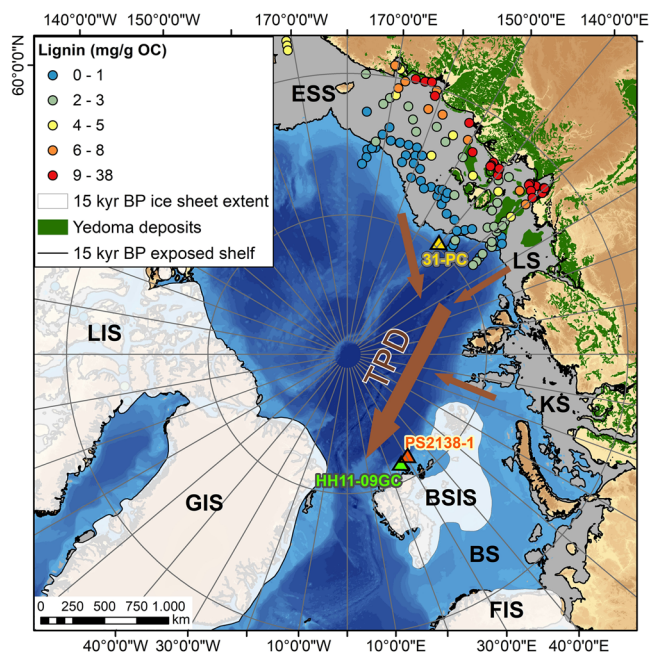

Fig. 1 Location of sediment cores and main geomorphological features. Base map represents bathymetry and morphology of the Arctic region (IBCAO V4[117]), with major Eurasian coastal seas indicated by their acronyms (BS Barents Sea, KS Kara Sea, LS Laptev Sea, ESS East Siberian Sea). Sediment cores HH11-09GC (this study), PS2138-1[33] and 31-PC[22] are shown as green, orange and yellow triangles, respectively. The extent of the major ice sheets of the northern hemisphere at ca. 15 kyr BP[46,118] (LIS Laurentide Ice Sheet, GIS Greenland Ice Sheet, BSIS Barents Sea Ice Sheet, FIS Fennoscandian Ice Sheet) is shown as partially transparent white areas. The grey area indicates the approximate extent of the exposed shelves at the onset of the B-A (without accounting for glacial isostatic adjustment). Green areas represent the current Yedoma deposit distribution[24], also showing its remnants on the shelf. Blue, green, yellow, orange and red dots on the continental shelves and slopes represent OC-normalized lignin content of surface sediment from the Circum-Arctic Sediment CArbon DatabasE (CASCADE)[69]. Brown arrows indicate the main directions of sea ice transport out from the continental shelves and their merging towards the TPD.

mainly because of the lack of past observational evidence and continuous records[29].

In this study, we present a multi-proxy analysis of a sediment gravity core (HH11-09GC) collected in the upper slope north of Nortaustlandet continental margin, Svalbard (Fig. 1 and Supplementary Fig. 1; 81°16'N, 26°13'E; core length 4.66 m; 488 m water depth[30,31]). This area is characterized by an exceptionally high sedimentation rate during the last deglaciation[30,32,33], which allows high-resolution paleoenvironmental reconstructions in a region where expanded, continuous records of the last Termination are rare. We combined a suite of terrestrial, marine and sea ice biomarkers (lignin phenols, cutin acids, *n*-alkanes, alkenones, highly branched isoprenoids and sterols) at high resolution, together with Compound Specific Radiocarbon Analyses (CSRAs) performed on individual high-molecular weight (HMW) *n*-alkanoic fatty acid methyl esters (FAMEs), to characterise the land-ocean connections during the last 30 kyr in response to natural climate change. Despite the lack of any direct riverine input proximal to the study area, we found an exceptionally high terrestrial biospheric contribution, starting when sea level rise was getting close to its maximum rate during the deglaciation (MWP-1A; Fig. 2a) and the climate signal from Greenland δ^{18}O was rapidly changing (Fig. 2b). To explain these findings, we
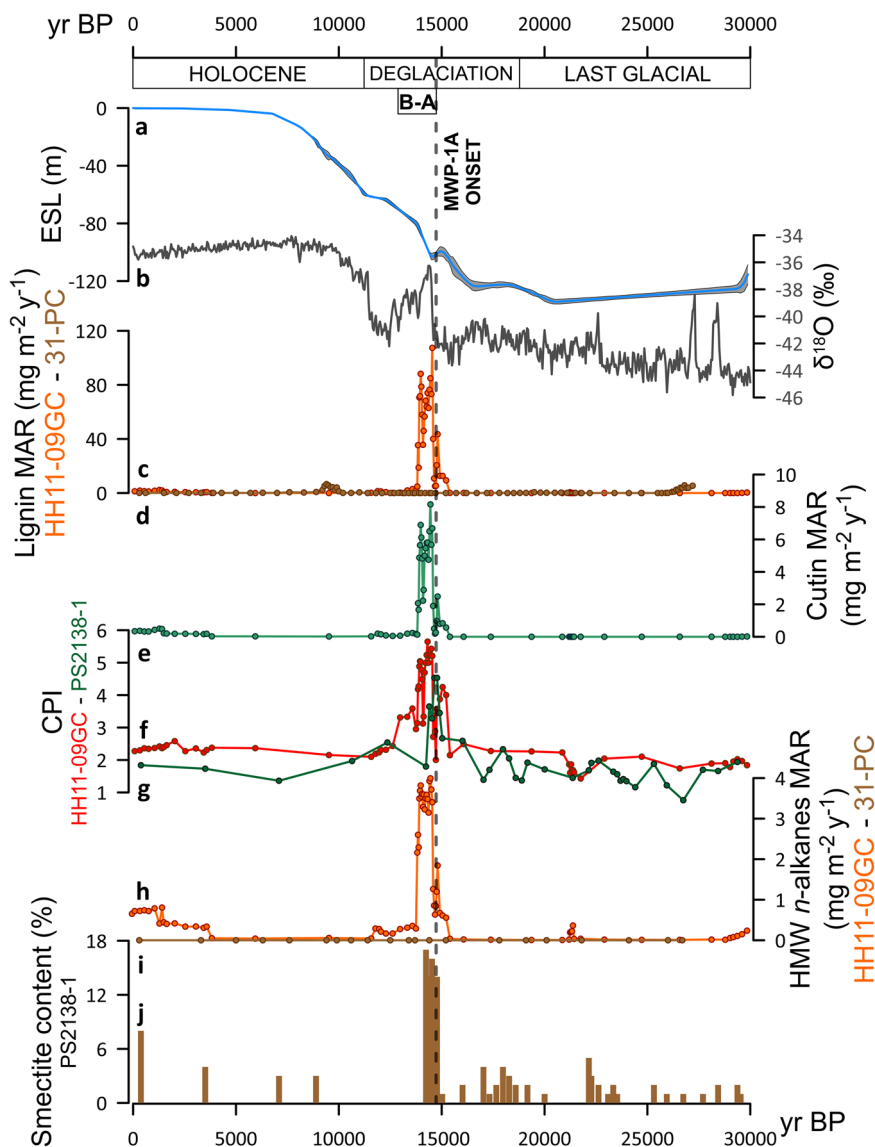
Fig. 2 Sedimentary record of abrupt terrestrial carbon deposition at the onset of the B-A. Main data plotted against calibrated age. **a** Estimated sea level curve (ESL, blue line), showing 1σ error bars as shaded area[102]. **b** Oxygen isotopes (δ^{18}O) from Greenland ice cores[119] (black line). **c** Lignin phenols Mass Accumulation Rate (MAR) from core HH11-09GC (orange line and dots) and (**d**) from core 31-PC (brown line and dots)[22]. **e** Cutin-derived products MAR (green line and dots) from core HH11-09GC. **f** CPI of *n*-alkanes from core HH11-09GC (red line and dots) and (**g**) from core PS2138-1[33] (green line and dots). **h** High molecular weight (HMW) *n*-alkanes MAR from core HH11-09GC (orange line and dots) and (**i**) from core 31-PC (brown line and dots)[22]. **j** Relative content of smectite in the clay fraction of core PS2138-1[33] (brown bars). The vertical dashed line displays the onset of MWP-1A.

considered four possible mechanisms: (A) a local source from Svalbard; (B) a pulse of freshwater discharge from the western Eurasian margin; (C) a transport process associated with the retreat of the Barents Sea Ice Sheet (BSIS); and (D) sea ice transport via the Transpolar Drift (TPD).

We used the gateway to the Arctic Ocean as a strategic region due to its relevance for sea ice export via the TPD (Fig. 1). Our final objective was to elucidate permafrost carbon reactivation mechanisms driven by abrupt climate warming and rapid sea level rise during MWP-1A. We also compared our dataset with other previously obtained records from the Eurasian Arctic, most notably from cores PS2138-1[33] and 31-PC[22] (Fig. 1). Specifically, the former, retrieved in the deeper part of the slope 80 km east of HH11-09GC, allows us to demonstrate that our record is not confined to a local effect, while the latter represents a valuable record from the Eurasian Arctic that covers the entirety of the last

Termination and for which terrestrial biomarkers have also been analysed at high resolution.

Results

HH11-09GC age-depth model and sedimentation rates. We developed a Bayesian age-depth model (Supplementary Fig. 2) with OxCal v4.4.4[34] based on 14 AMS radiocarbon dates calibrated using Marine20[35]. The radiocarbon dates include 13 foraminiferal tests and one bivalve shell (Supplementary Table 1), of which 5 have been analysed in the current study and 9 published previously by Chauhan et al. [30]. The near surface ΔR values used here for reservoir correction were obtained from the work of Brendryen et al. [5] (see section "Radiocarbon dating and age-depth model" in Materials and Methods for details) in the Norwegian Sea, which affects surface waters entering the Arctic Ocean

(an analogous approach was used by Keigwin et al. for the Beaufort Sea[36]). Here we focused on the uppermost section of the core (3.35 m), which spans from ca. 31.5 kyr BP to the present day. Our age-depth model suggests that, during the glacial period (30.0–19.0 kyr BP), sedimentation rates were relatively low (~0.01–0.02 cm yr^{-1}; Supplementary Fig. 3b), apart from a short period coinciding with the LGM (up to 0.08 cm yr^{-1}). The onset of the deglaciation was also characterized by low sedimentation rates followed by a rapid increase to ~0.1 cm yr^{-1} in the interval between 14.8 and 13.8 kyr BP (almost one third of the considered core section in length). After 13.8 kyr BP, sedimentation rates decreased again featuring low values (~0.01–0.02 cm yr^{-1}), consistent with those found typically in the study region over the Holocene[33,37].

Biospheric deposition at the B-A transition. We quantified lignin phenols and cutin acids, a suite of biopolymer-derived monomers, which are found, respectively, in the main structure of vascular plants and in leaf waxes of soft plant tissues (i.e., needles and leaves), and can thus be used as tracers of the input of terrestrial biospheric material[38,39]. Between 30.0 and 15.2 kyr BP both biomarkers display extremely low mass accumulation rates (MARs) (Fig. 2c–e), indicating the virtual absence of biospheric input from land, likely due to the absence of widespread vegetation across the Svalbard archipelago[40,41] and the large distances from river outlets. The MAR of HMW n-alkanes (C_{23}-C_{33}), another proxy of terrestrial biospheric contribution, shows consistent results (Fig. 2h). Similar background values for lignin and n-alkanes, during the LGM, are also found on the Laptev Sea lower slope on the Lomonosov Ridge (sediment core 31-PC; Figs. 1 and 2d–i)[22]. Between 30.0 and 15.2 kyr BP, the Carbon Preference Index (CPI; Eq. 1 in Supplementary Material), an index based on the ratio of odd-over-even n-alkanes, shows low values (ca. 1.8; Fig. 2f) consistent with modern sediments from Svalbard's fjords[42] and with the widespread presence of fossil OC-rich units in Svalbard[43]. In fact, low CPI values are usually distinctive of old reworked OC and bedrock-derived material with thermally mature organic material (OM)[44] (i.e., CPI close to 1). Alternatively, this could be evidence of highly degraded terrestrial material that experienced long-range transport, not least since the study region is disconnected from any direct river input. The only noteworthy event registered in the core before 15 kyr BP is the deposition of a 40 cm thick sandy interval[30] around 22 kyr BP with low terrestrial biomarker and OC content (Fig. 2; Supplementary Fig. 3c). This likely corresponds to the maximum advance of the BSIS on the continental shelf[45–47] and to the subsequent remobilization of material that accumulated on the upper slope. Overall, before 15 kyr BP, the depositional environment is characteristic of polar continental margins[48], with a strong influence of the BSIS that resulted in the deposition of mainly glacially-eroded material. After this interval, the impact of the BSIS on the site gradually weakened as the grounding line retreated more inland.

After several millennia of relatively small changes in OC deposition, the content of terrestrial biospheric material increased substantially around 15 kyr BP, notably within the B-A unit (Fig. 2c–h). Specifically, lignin, cutin and HMW n-alkane MARs increased by two orders of magnitude, along with an increase in CPI values (ranging from 3 to 6). A comparison with data obtained from other Arctic continental margins reveals that these terrestrial-derived biomarkers reached concentrations (4–10 mg g^{-1} OC for lignin; Fig. 3c) commonly observed in inner shelf areas of the river-dominated Siberian margin[39,49] (Fig. 1). A similar event was also found in a previous study from core PS2138-1[33] located proximal to our record (Fig. 1). Despite the lower resolution, the authors

were able to identify a clear peak in the CPI (values between 3 and 4) during the deglaciation (Fig. 2g). By recalibrating the ^{14}C ages (see section "Radiocarbon dating and age-depth model" in Materials and Methods) for core PS2138-1 reported in Matthiessen et al.[37], the terrestrial biospheric input occurred coeval among the two cores (Fig. 2f, g). A follow-up study on PS2138-1[32] focused on the clay mineral assemblages to better define the origin of this exotic material, and an increase in smectite content during the same time span was identified (Fig. 2j). Smectite is an uncommon clay mineral around the Svalbard archipelago, with potentially significant sources further east[50–52], indicating that this material likely travelled several thousands of kilometres prior to its deposition at the gateway to the Arctic Ocean. Interestingly, lignin and HMW n-alkanes MARs recorded in core 31-PC show, in contrast, much lower values (by 2–3 orders of magnitude) for the entire deglaciation (Fig. 2d–i).

Finally, following the relatively short period of intense terrestrial OC deposition identified in HH11-09GC (ca. 15.2-13.8 kyr BP), the late deglaciation and the entire Holocene were characterised by a low accumulation of biospheric carbon, as expected for a core site far from any direct river input. Lignin concentration (on average 0.35 mg g^{-1} OC) and CPI (on average 2.3) display values slightly higher than during the glacial period, suggesting a small contribution from Holocene vegetation, noticeably degraded, mixing with the locally sourced bedrock material.

Organic carbon characteristics and environmental parameters. Alkenones are unusual algal lipids biosynthesized by certain phytoplanktonic microorganisms, whose distribution is traditionally used for paleo sea surface temperature reconstructions[53,54]. In the polar regions, the concentration of the MeC$_{37:4}$ alkenone relative to those of MeC$_{37:2}$ and MeC$_{37:3}$ (Eq. 3 in Supplementary Material) has also been used as a proxy for paleo salinity to infer freshening episodes driven by changes in the cryosphere[53,55]. More recently, the MeC$_{37:4}$ alkenone has also been identified in Isochrysidales algae associated with sea ice[56], while the Arctic strain of *Gephyrocapsa huxleyi* produces large amounts of MeC$_{37:4}$ in nutrient-rich conditions[57]. In our HH11-09GC record, the relative concentrations of MeC$_{37:4}$ and other tetra-unsaturated alkenones (i.e., EtC$_{38:4}$ and MeC$_{38:4}$) follow the same general trend observed with lignin and cutin content (Fig. 3b–e), implying that a common mechanism could explain both sets of biomarkers. In general, EtC$_{38:4}$ and MeC$_{38:4}$ alkenones are more typical of freshwater systems[53,58,59] and were not observed in Isochrysidales algae. Indeed, MeC$_{38:4}$ (Eq. 4 in Supplementary Material), which is relatively abundant in the B-A section compared to the Holocene (Fig. 3e), is dominant in freshwater organisms[60]. To investigate this further, we quantified IP$_{25}$, a mono-unsaturated Highly Branched Isoprenoid (HBI) biomarker derived from some Arctic sea ice algae[61] and HBIs III and IV, which are produced by different diatoms that inhabit the open waters of the Marginal Ice Zone (MIZ)[62,63]. Between ca. 30 and 15 kyr BP, IP$_{25}$ and HBIs III and IV are virtually absent (Fig. 3g–i), indicating that the core site was likely under a perennial ice cover[62]. This conclusion is corroborated by the observation of exceptionally low concentrations of brassicasterol (Fig. 3f), a ubiquitous biomarker produced by marine phytoplankton[64].

Overall, IP$_{25}$ concentrations do not exhibit any clear correlation with terrestrial biomarkers (Supplementary Fig. 4) or with the relative abundance of the MeC$_{37:4}$ alkenone, further suggesting that tetra-unsaturated alkenones in HH11-09GC were not derived from a sea ice source. IP$_{25}$ values started to increase around 15.5 kyr BP before reaching a peak at 14.8 kyr BP (Fig. 3g), which corresponds to a minimum in the terrestrial influence. Following a period of lower IP$_{25}$ content, values increased again towards the Holocene,
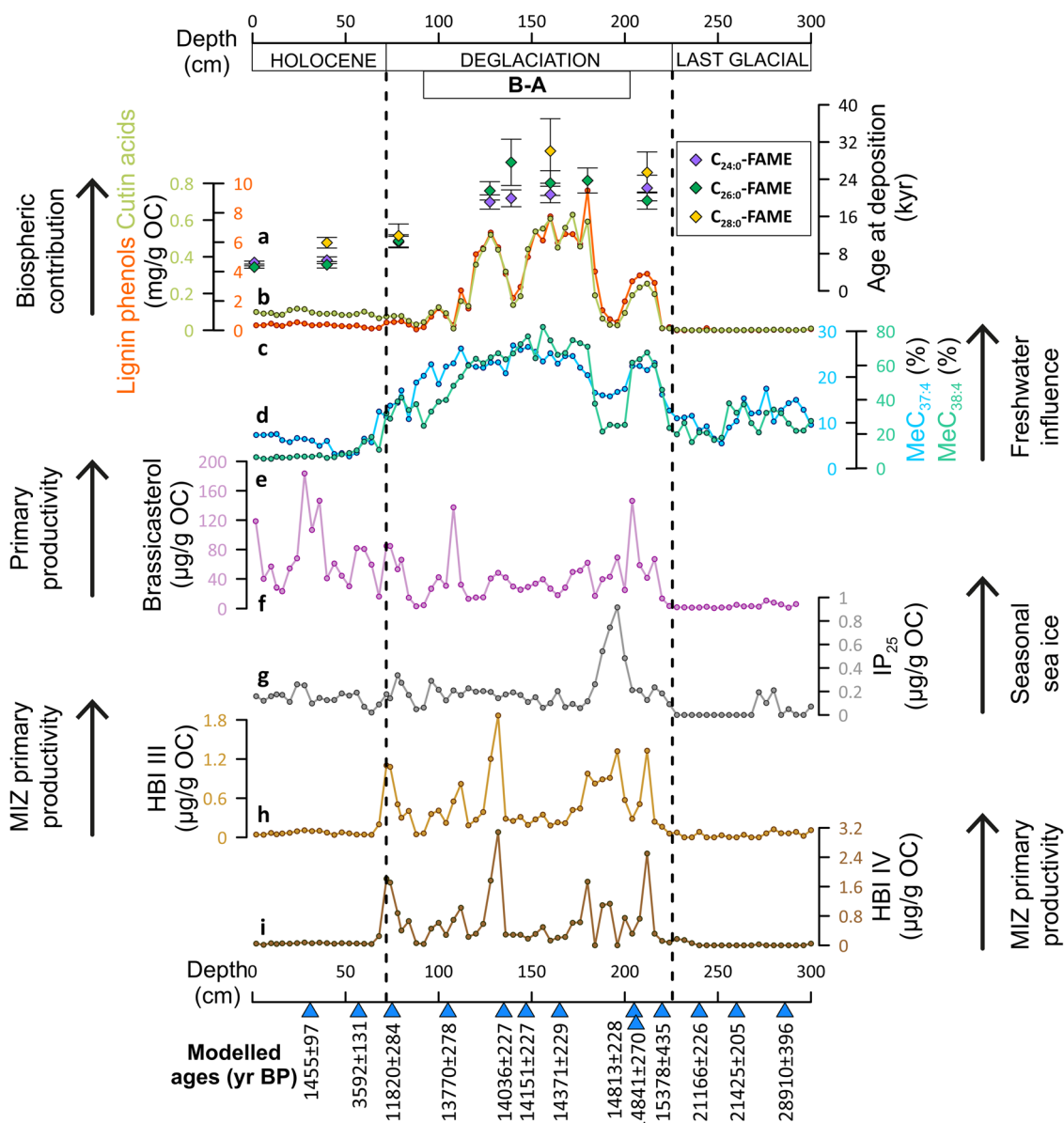
Fig. 3 Biomarker fingerprint of the exotic organic material. Main data from core HH11-09GC plotted against the core depth to ensure a better visualization of the extended deglaciation record. **a** Compound specific radiocarbon pre-depositional ages for terrestrial $C_{24:0}$, $C_{26:0}$, $C_{28:0}$ FAMEs (purple, green and yellow dots respectively) with 1σ error bars; OC-normalized concentration of (**b**) cutin acids (green line and dots) and (**c**) lignin phenols (orange line and dots); relative abundances of (**d**) $MeC_{37:4}$ (light blue line and dots) and (**e**) $MeC_{38:4}$ alkenone (aqua green line and dots) referred to MeC_{37} and MeC_{38} groups respectively. **f** OC-normalized concentration of brassicasterol (light purple line and dots); OC-normalized concentration of (**g**) IP_{25} (grey line and dots), (**h**) HBI III (light brown line and dots) and (**i**) HBI IV (brown line and dots). The vertical dashed lines highlight the temporal division between Holocene, deglaciation and the last glacial period. Blue triangles and numbers at the bottom represent median values of 13 modelled dating points with 1σ uncertainty (for visualization purposes, the lowest age is not displayed in this plot because its core depth exceeds 300 cm). Black arrows and texts on both sides of the graph indicate what each corresponding biomarker is associated with.

probably reflecting the establishment of modern sea ice conditions[65,66]. HBIs III and IV display somewhat variable values throughout the deglaciation (Fig. 3h, i), likely reflecting changes in sea ice dynamics (*cf.* IP_{25}) and/or in the contributions from in situ production and laterally advected material.

To further characterize the source of terrestrial OC, CSRAs were carried out on individual isolated long-chain FAMEs of terrestrial origin (i.e., $C_{24:0}$, $C_{26:0}$ and $C_{28:0}$) deposited during the deglaciation and the Holocene. For the LGM unit, the concentration of FAMEs was too low to obtain reliable age estimates. Figure 3a shows the compound specific radiocarbon pre-depositional ages in kyr,

obtained from the absolute radiocarbon ages corrected for the age at deposition (see Supplementary methods). The oldest pre-depositional ages (>25 kyr) were measured during the deglaciation, primarily in correspondence with the high terrigenous OC flux during the B-A. These ages imply the deposition of heavily pre-aged terrestrial OC or, alternatively, a mixture of relatively young terrestrial pools with ancient terrestrial OC sources. During the Holocene, pre-depositional ages of FAMEs become younger, showing an average value of ca. 7 kyr, which is closer to values observed along Arctic margins (ca. 4 kyr in the Northern Pacific sectors[67] and in the major Russian Arctic rivers[68]).

Discussion

Collectively, our multi-biomarker analysis provides compelling evidence for an unprecedented input of pre-aged terrestrial carbon and, more specifically, biospheric material at the gateway to the Arctic Ocean during the B-A warm period, consistent with the onset of MWP1-A. Indeed, both the composition and concentration of this material show characteristics more commonly associated with inner-shelf sediments of terrigenous-rich, river-dominated Arctic margins[39,69], which do not correspond to the expected depositional settings of the core site, located in the high Arctic. Such a finding, therefore, raises questions about the mechanisms behind the release of this pre-aged terrestrial OC and whether the high terrigenous deposition can be attributed to rapid climate change and sea level rise during the B-A.

Given the different pathways for land-to-ocean transport in the Eurasian Arctic during the B-A, we considered four possible mechanisms to explain the delivery of ultra-high terrigenous OC to the core location: (A) local Arctic material from the Svalbard archipelago, remobilized and transported by the BSIS ice streams; (B) freshwater discharge from the western Eurasian margin in response to the ice sheet retreat; (C) transport of land-derived material via a meltwater outburst involving the BSIS collapse; and (D) advection and melting of sediment-laden sea ice via the TPD. To evaluate each of these, we interpreted our combined biomarker findings alongside sediment properties and previous literature data.

Firstly, hypothesis A, regarding local sources of OM driven by the BSIS, can be easily discarded as an explanation, owing to the Svalbard archipelago being extremely devoid of vegetation prior to the deglaciation. Even in modern times, in a warm interglacial, the dominant bioclimatic subzones in Svalbard include tundra, moss-dominated tundra and polar desert[70,71]. In fact, the modern vascular plant contribution to our study region, estimated as lignin contents in the archipelago soils (average value ca. 0.4 mg g^{-1} OC, which declines to ca. 0.1 mg g^{-1} OC in surface sediment of fjord coasts[40,41]), is well below the lignin concentration measured in the B-A unit (4–10 mg g^{-1} OC). The high CPI of n-alkanes in the B-A unit also argues against a significant contribution from metamorphic local bedrock units[43] (CPI values around 1[72]) and glacier erosion-derived supply. This is further supported by CSRAs, which exclude the presence of primarily radiocarbon dead material - despite it being highly pre-aged - that would be the major fingerprint of bedrock-derived material. Finally, the absence of a well-developed trough mouth fan system in the Albertini Trough[73] where the core was retrieved, as well as the presence of coarse IRDs limited to around 14.7-14.6 kyr BP during the terrigenous OC minimum, are not consistent with a significant influence from ice sheet dynamics (Supplementary Fig. 5).

The rejection of a locally-sourced terrestrial OC pool to HH11-09GC during the B-A implies a long-range transport from a distal source. Hypothesis B, regarding supply by Eurasian rivers and redistribution through sediment transport processes, seems unlikely, because more than 1500 km separate the core location from the closest Eurasian coastline. In fact, upon release into the coastal system, lignin and cutin experience intense degradation during sediment transport over the Arctic margins until final burial in sediments[49,74] (e.g., Siberian margin; Fig. 1). Such degradation is believed to be a consequence of the protracted oxygen exposure during transport[49,74]. For the B-A unit, our data suggest an opposite scenario, with rapid burial of land-derived material and minimal degradation, as corroborated by lignin-based degradation proxies, indicating that samples with higher lignin concentration show minimal signs of degradation (Supplementary Fig. 6). In addition, the sediment transport pathway is unlikely, given the bathymetry, as the material would have needed to bypass major troughs (e.g., St. Anna trough, with

a maximum depth of more than 600 m) to reach the core location. Furthermore, the pre-depositional age of the FAMEs within the B-A unit is much older than the material supplied by modern Arctic rivers (up to ca. 8 kyr), including those located in continuous permafrost[68].

Thirdly, one might potentially envisage temporary storage in a proglacial basin inland (e.g., around the White Sea area) for at least 20 kyr, followed by a large meltwater discharge as the BSIS was retreating at the onset of the B-A (hypothesis C). However, in addition to the presence of major troughs and the labile nature of terrigenous biomarkers described previously, the terrestrial material is significantly older than the maximum extent of the BSIS towards the LGM[45,46,75], when the entrapment of land-derived material would have presumably occurred. In fact, the absolute age of FAMEs, without correcting for the time of deposition, reaches up to ca. 45-35 ^{14}C kyr (Supplementary Table 2), when the continental shelf was mostly ice free[46,76,77].

Along with the hypothesis C, a scenario involving a subglacial transport associated with the rapid retreat of the BSIS during the B-A[5] could certainly explain the extremely high sedimentation rate given the short distance from the BSIS edge. However, this would require the formation of a proglacial lake along the southern margin of the BSIS and the subsequent subglacial accumulation of riverine and lacustrine material from inland beneath the ice sheet, followed by subglacial transport across the entire BSIS from south to north. From a purely mechanical perspective, however, previously published hydraulic gradient maps[78] and past subglacial flow direction indicators[79] are inconsistent with a land-to-ocean connection across the ice sheet[78], not least since, to achieve this, the material would need to overcome the ice divide of the BSIS and move against the hydraulic gradient to reach northern Svalbard.

Finally, we evaluated hypothesis D, concerning the transport of biospheric OM to HH11-09GC via sediment-laden sea ice, which stands as our preferred explanation. This scenario implies an active advection via the TPD, as seen in modern times, that projects sea ice from the Siberian shelves and regions further east towards the Fram Strait[32,80–83] (Fig. 1). The presence of sea ice is especially evident from the continuous presence of IP$_{25}$ after ca. 15 kyr BP (Fig. 3g), following virtual absence during the LGM. It is also well-known that sea ice forming along the Arctic coastline can incorporate heterogeneous particles, including riverine material containing plant remnants, terrigenous-rich sediments and freshwater algae[83,84], depending on the environment and physiography of the area[83,85]. For example, Wegner et al.[83] showed that about 20% of the diatom assemblages in sea ice collected within the TPD derived from freshwater systems, and this provides a plausible explanation for the relatively high tetra-unsaturated alkenone fingerprint in the terrigenous-rich B-A unit (Fig. 3d, e), that follows the general lignin and cutin trend. In addition, the relatively fine-grained sediment texture and the paucity of coarse IRDs[30] (Supplementary Fig. 5) corroborate hypothesis D, especially considering the silty-type sediments most commonly transported by sea ice[86,87]. Transport via sea ice also explains the absence of significant degradation of the terrestrial OM found in the B-A unit (Supplementary Fig. 6). Assuming suspension freezing could be, as today[88], the main process for the entrainment of particles inside sea ice, this implies the partial isolation of OM from oxygen exposure, which is the main driver of degradation in the marine environment[39,49]. Further, this transport mechanism is relatively rapid (only a few years are necessary for sea ice to travel from Siberian shelves towards the Fram Strait[89]) and does not entail intermediate deposition sites, where the material could undergo degradation.

Under this sea ice transport and melting scenario, the development of a MIZ-like environment for a large part of the

deglaciation[63] likely explains the increase in the open water biomarkers brassicasterol and HBIs III and IV, as a consequence of higher marine primary productivity stimulated by nutrients released from melting sea ice[90,91], which could also promote the synthesis of larger amounts of the $MeC_{37:4}$ alkenone in the Arctic strain of *Gephyrocapsa huxleyi*[57]. Lastly, the relatively high percentage of smectite in the clay fraction measured in the nearby core PS2138-1 is a clear indication of the sediment provenance, which rules out a local source from Svalbard[52], instead pointing to sources further east including the Kara and Laptev Sea shelves[32,50]. We also believe that the lack of a clear increase in the sea ice proxy IP_{25} within the terrigenous OC-rich unit indicates that this event was characterised by a significant increase in the number of sediment particles bound to sea ice during this time (i.e., sediment-laden sea ice), rather than by an increase in the sea ice export per se. In fact, several previous studies that focused on sea ice reconstructions of glacial and deglacial periods around the Fram Strait and the Northern Barents Sea[66,92,93] do not point to particularly high sea ice presence and export at the onset of the B-A.

Recent estimates[94,95] show that the modern average annual sea ice export through the Fram Strait is on the order of 2500 km³, with a total annual sediment export of ~160 Tg[86]. This corresponds to an average sediment particle concentration of ~60 g m⁻³, which falls within the lower range found in discrete sea ice samples documented in the literature (between 10 and 56000 g m⁻³)[85]. Consequently, if the higher limit for sediment concentrations in sea ice were replicated, or even exceeded, during the B-A, it becomes reasonable to propose that sediment-laden sea ice export from the Eurasian Arctic could readily have been responsible for generating the observed deposit.

Despite several lines of evidence pointing towards a sediment-laden sea ice transport mechanism, two aspects remain to be explained, namely (a) the reason why sea ice entrained so much sediment during the B-A and (b) the source of the material. Our hypothesis is that, during MWP-1A, sea level rise massively enhanced coastal erosion[96–98] resulting in the entrainment of large volumes of coastal deposits within newly formed sea ice. CSRAs of the terrestrial biomarkers indicate that the material was pre-aged at deposition with an overall age of formation consistent with MIS 3. The coastal Yedoma deposits documented around the Siberian and Alaskan margins[17,99] (Fig. 1) display radiocarbon ages that align very closely with the ages measured in the B-A unit[24,100]. In addition, lignin-based proxies enable us to discriminate between different sources (i.e., woody vs non woody material and angiosperm vs gymnosperm tissues) based on the ratios of syringyl and cinnamyl phenols over vanillyl phenols[39,101] and the fingerprint of the B-A unit is compatible with a Yedoma signature (Supplementary Fig. 7). Coastal Yedoma deposits are known to be highly susceptible to instability due to their high ice content, with modern erosion rates reaching several meters per year[27,28]. We could therefore propose that MWP1-A (with a sea level rise of almost 18 m in less than 500 y[6,102]) corresponded to a period of exceptional Yedoma erosion. Furthermore, the B-A is also known for the general reorganization of the AMOC, which resulted in an enhanced transport of heat towards the northern Hemisphere[8,103], including the Arctic Ocean. We therefore propose that sea ice melting, sustained by the warm Atlantic inflow, promoted the deposition of sea ice-advected sediments at the boundary between the Atlantic and Arctic domains.

Prior to the current study, none of the previous Arctic reconstructions dealing with permafrost remobilisation during past warming events have documented the massive erosion of Yedoma during MWP-1A. For example, sediment core 31-PC from the Lomonosov Ridge[22] (Fig. 1) failed to capture this event in both magnitude and timing. Specifically, fluxes of terrestrial biomarkers measured in the 31-PC record are, if compared to our B-A unit, 2 to 3 orders of magnitude lower (Fig. 2d–i) (see also Supplementary Material in Martens et al.[22], Fig. S2c). The reason behind the weak influence of sea ice-driven sediment deposition in 31-PC could be that the core site was positioned north of the sea ice edge during the sea ice minima, as seen in the modern satellite record (1979-2010) prior to the recent retreat further north[104]. In fact, most of the modern sea ice melting occurs further west within the Fram Strait, which accounts for 90% of Arctic sea ice outflow[95]. The resulting heat loss driven by sea ice melt in the Fram Strait and Nordic Sea region is around 115 TW, compared to 16 TW in the entire Arctic Ocean[105], further confirming the different impact of sea ice dynamics between regions. The 31-PC sediment core location was also probably too deep (1120 m water depth) to be directly influenced by coastal erosion and sediment transport mechanisms (Fig. 1) and the material deposited in HH11-09GC was potentially sourced from locations further east or west. In any case, a survey of the recent literature describing past permafrost dynamics in the Arctic Ocean clearly indicates that previous reconstructions are partially discontinuous and, in several cases, only start after the B-A period, and, therefore, do not document past changes to Yedoma stability during MWP1-A[106,107].

Conclusions

The role of sea level rise in coastal permafrost erosion during the last deglaciation was first documented in the North Pacific by Winterfeld et al. in 2018[15]. However, while in this region the source of coastal permafrost was proximal to the sediment core location, our study area is located far from any direct land-to-ocean conduit. Thus, this highlights the severe impact that MWP-1A must have had on the Yedoma stability along the flooded Arctic margin. Today, coastal erosion of Yedoma-like ice-rich permafrost in the Arctic Ocean is a widespread phenomenon[27,28], with average erosion rates on the order of 0.5–0.7 m yr⁻¹ and extremes >25 m yr⁻¹[27,108,109]. However, the magnitude of sediment-laden sea ice export documented in this study is far from that described in modern studies. We therefore infer a scenario of unprecedented coastal erosion during MWP1-A, capable of producing a Yedoma-rich unit at the gateway to the Arctic Ocean through the export of sediment-laden sea ice within the TPD.

Previous modelling studies and indirect evidence from coral records[25,26] have suggested that flooding of the Siberian margin and erosion of coastal permafrost deposits could have affected deglacial atmospheric CO_2 increase. Yedoma deposits, including the exposed Arctic continental shelves during the last glacial period, potentially accounted for 657 ± 97 Pg C susceptible to mechanical and thermal destabilization[24]. In particular, MWP1-A has been proposed as a key period for the release of CO_2 from collapsing permafrost, with atmospheric CO_2 concentration increasing by 12 ± 1 ppm[2], despite the absence of empirical evidence of sea level-Yedoma interactions[25]. Other studies, dealing with the reorganization of permafrost-carbon soils during the LGM-Holocene transition, have instead assumed virtually stable Yedoma domains over the shelf despite the post-glacial sea level rise[19]. Our reconstruction, in this respect, represents a fundamental benchmark as it provides a mechanistic understanding of the processes driving permafrost release during rapid sea level rise and, thus, it offers new conceptual frameworks for future models and permafrost carbon budgets. In particular, we provide compelling evidence from the Arctic Ocean about the interaction between sea level rise and coastal Yedoma erosion, accurately constraining its timing during MWP1-A[2]. Further investigations

from the Greenland Sea, Fram Strait and Nordic Seas are needed to corroborate the large-scale nature of this event and, ultimately, elucidate the response of permafrost to rapid sea level rise and warming.

Methods

Subsampling and pretreatment. Sediment core HH11-09GC was subsampled at 2-cm resolution and a total of 149 samples were collected from the upper 300 cm of the core. Chauhan et al.[30,31] subsampled at 2-cm resolution for grain size analyses, at 5-cm resolution for bulk geochemical analyses and at 5-, 2- and 1-cm resolution, depending on the core section, for micropaleontological and IRD analyses (115 samples in total over the entire 466 cm core).

Sediments for the current study were freeze-dried, ground for homogenization and stored in glass vials prior to geochemical analyses at the Institute of Polar Sciences of the National Research Council in Bologna, Italy.

Radiocarbon dating and age-depth model. A total of 14 radiocarbon dates on calcareous marine organisms were used in this study (Supplementary Table 1), of which 9 were retrieved from the literature[30]. 5 radiocarbon dates were measured at the AWI-MICADAS facility[110] in Bremerhaven, Germany (4 samples) and at the US-NSF NOSAMS facility in Woods Hole, USA (1 sample). Radiocarbon dates were calibrated using the Marine20 calibration curve[35] and the age-depth model was generated using a *P Sequence* model in OxCal v4.4.4[34]. We applied a variable regional marine reservoir correction (ΔR) to each ^{14}C date following the marine radiocarbon reconstruction for the Norwegian Sea published in Brendryen et al.[5]. The ΔR value for each ^{14}C determination was estimated as the difference between the Normarine18 radiocarbon age[5] and its counterpart on Marine20[35] using linear interpolation. Beyond the Normarine18 calibration period (i.e., before 21 kyr BP), we applied the lowermost assessable ΔR correction, that is ca. 170 years.

We employed the same approach to recalibrate and construct an age-depth model for the radiocarbon dates of sediment core PS2138-1[37]. For both sediment sequences, the age output shows a robust and coherent age model as indicated by high agreement indices, with values higher than 98% (i.e., well above the critical threshold of 60%[34]).

Bulk data and biomarkers. Bulk data, in the form of total organic carbon (TOC) and total nitrogen (TN) content, were measured in all 149 samples via EA-IRMS (Elemental Analyzer-Isotope Ratio Mass Spectrometry). Around 20 mg of grounded sediment was acidified with diluted HCl (1.5 N) in silver capsules to remove inorganic carbonates. Analyses were then performed by a Finnigan Delta Plus XP mass spectrometer coupled with a Thermo Fischer Scientific FLASH 2000 Elemental Analyzer as described by Tesi et al.[111].

Out of the total 149 samples, 77 were then analyzed for specific biomarkers (4-cm resolution).

Lignin phenols and cutin acids were analyzed via CuO oxidation following the method published by Goñi and Montgomery[112]. Around 250-300 mg of sediment were oxidized in a 2 M NaOH aqueous solution under oxygen-free conditions in Teflon vessels using CEM Mars6 Microwave Digestion System (150 °C for 90 min). After the oxidation, the samples were transferred into Falcon tubes and a known amount of internal standard (ethylvanillin) was added to each sample to estimate recovery rates. Samples were centrifuged and then the liquid phase was transferred into pre-combusted glass tubes. The solution was acidified (pH=1) with concentrated HCl and

extracted twice with ethyl acetate. The extracts were filtered with anhydrous Na_2SO_4 to remove excess water, dried under N_2 stream and redissolved in pyridine. Samples, prior to the analysis, were derivatized at 50 °C for about 30 min with N,O-Bis(trimethylsilyl)trifluoroacetamide (BTSFA) with 1% trimethylchlorosilane (TMCS). The quantification of CuO oxidation products was performed via gas chromatography-mass spectrometry (GC-MS), using an Agilent 7820 A Gas Chromatograph coupled with a 5977B Mass Selective Detector in single ion monitoring (SIM), equipped with a Trajan SGE 30 m × 320 µm (0.25 µm-thick film) PB-1 capillary column. The oven temperature ramp was set from 95 °C to 300 °C at a rate of 4 °C/min with a hold time of 10 min.

CuO oxidation products analyzed include (a) 3,5-dihydroxybenzoic acid, (b) 8 lignin phenols: vanillyl (V) (vanillin, acetovanillone, vanillic acid), syringyl (S) (syringealdehyde, acetosyringone, syringic acid) and cinnamyl (C) phenols (p-coumaric acid, ferulic acid) and (c) 8 cutin acids: 16-hydroxyhexadecanoic acid, hexadecan-1,16-dioic acid, 18-hydroxyoctadec-9-enoic acid, 7 or 8-dihydroxy C_{16} α,ω-dioic acid and 8, 9 or 10 16-dihydroxy C_{16} acids[38,112]. Quantification of lignin phenols was achieved through calibration curves obtained from commercially available standards (Sigma-Aldrich). Cutin acids were quantified against the concentration of the internal standard. We reported the total lignin concentration as the sum of the 8 lignin-derived phenols and the total cutin concentration as the sum of the 8 cutin acids.

Hydrocarbons (HBIs and *n*-alkanes) and algal lipids (sterols, alkenones) were extracted following a slightly modified method from Tesi et al.[113]. A known amount of internal standards (7-hexylnonadecane, 9-octylheptadec-8-ene, docosane, 5α-Androstan-3β-ol) was added to ~1.5 g of sediments. Samples were left in a 5 wt% KOH, $MeOH:H_2O$ (9:1 v/v) solution at 70 °C for 1 h to complete saponification. The neutral fraction was then extracted from the aqueous solution three times, after centrifugation, with pure hexane (HEX). Extracts were dried under N_2 stream and redissolved in HEX:DCM (3:2 v/v). Purification was performed using silica gel (60–200 µm) column chromatography. The apolar fraction (containing HBIs, *n*-alkanes and alkenones) was eluted with HEX:DCM (3:2 v/v) and the polar fraction (containing sterols) with MeOH:DCM (1:1 v/v). The polar fraction was then redissolved in DCM and, prior to GC-MS analysis, subsampled and derivatized with BTSFA with 1% TMCS.

We then followed the method developed by Rontani et al.[114] to quantify alkenones in small concentrations via GC-MS. The apolar fraction was redissolved in MTBE:MeOH (3:1 v/v) with an excess $NaBD_4$ and left at room temperature for an hour to transform alkenones into alkenols. Excess $NaBD_4$ was then neutralized by adding NH_4Cl-saturated ultrapure water. The aqueous solution was subsequently acidified with concentrated HCl and extracted with HEX:DCM (4:1 v/v). Reduced extracts were dried under N_2 stream, redissolved in pyridine and derivatized with BTSFA with 1% TMCS for GC-MS analysis.

The analyses of both apolar and polar fractions were performed via GC-MS, using an Agilent 7820 A Gas Chromatograph coupled with a 5977B Mass Selective Detector in SIM, equipped with a Trajan SGE 30 m × 320 µm (0.25 µm-thick film) PB-1 capillary column. For the analyses of the entire apolar fraction, the oven temperature ramp was set from 60 °C to 250 °C at a rate of 10 °C/min, and then up to 300 °C at a rate of 4 °C/min, with a final hold time of 25 min. For the analyses of the polar fraction, the oven temperature ramp was set from 70 °C to 200 °C at a rate of 8 °C/min, and then up to 300 °C at a rate of 4 °C/min, with a final hold time of 10 min.

The analyzed compounds included (a) IP_{25}, HBI II, III and IV, (b) C_{15} to C_{35} *n*-alkanes, (c) brassicasterol, cholesterol, sitosterol and campesterol, and (d) $MeC_{37:2}$, $MeC_{37:3}$, $MeC_{37:4}$, $MeC_{38:2}$,

MeC$_{38:3}$, MeC$_{38:4}$, EtC$_{38:2}$, EtC$_{38:3}$, EtC$_{38:4}$, EtC$_{39:2}$, EtC$_{39:3}$ alkenone-derived alkenols. HBIs were quantified with the method presented in Belt et al.[61] for the IP$_{25}$, applying it also for HBI III and IV. The SIM peak areas of the individual HBIs were correlated with the SIM peak areas of the internal standard and a response factor was applied to account for the differences in mass spectral responses. Alkanes were quantified using commercially available external standards after correcting for the internal standard. Alkenones were quantified by converting the SIM results to total ion chromatogram (TIC) results using a correction factor (obtained by the analysis of concentrated samples over different concentrations) and comparing them to the response of the internal standard. Relative abundances of methyl C$_{38}$ and ethyl alkenones, due to co-elution problems impeding the conversion of their SIM peak areas into TIC, have been calculated based on the integrated peak areas from SIM mode only. Results of the quantified compounds are shown as both MARs (Mass Accumulation Rates) and OC-normalized data.

Compound specific radiocarbon analyses (CSRA). CSRA data were obtained from specific high molecular weight *n*-alkanoic acids. We integrated different ranges of sediment depths (Supplementary Table 2) in order to collect a sufficient amount of material for the analysis (at least 100 μg of the selected compounds are necessary for radiocarbon dating). The different integrated depth for each sample corresponds, on average, to a period of 75 years according to our age-depth model. Taking into account that the analytical uncertainty on the ^{14}C age of the individual compounds is on average ca. 2000 years, we thus considered the uncertainty caused by the sediment depth integration as negligible.

Around 100 g of sediment was extracted for 48 h with a Soxhlet system using a DCM:MeOH (9:1 v/v) mixture. Extracts went through saponification with a 0.1 M KOH solution (MeOH:H$_2$O, 9:1 v/v) for 2 h at 80 °C. The aqueous solution was acidified to pH = 1 with concentrated HCl and extracted 3 times with HEX. Samples were dried under N$_2$ stream and methylated at 80 °C overnight with HCl and MeOH (with a known ^{14}C signature). The resulting FAMEs were extracted 3 times using HEX and separated from the polar fraction via silica gel column chromatography. Specific FAMEs were isolated and purified via Preparative Capillary Gas Chromatography (PC-GC)[115] with an Agilent HP6890N GC coupled with a Gerstel Preparative Fraction Collector and a Restek Rxi-1ms fused silica capillary column (30 m, 0.53 mm diameter, 1.5 μm film thickness). The purity and recovery of each FAME fraction were then checked via Gas Chromatography – Flame Ionization Detection (GC-FID).

Purified FAMEs were subsequently transferred into 25 μL tin capsules using a minimum amount of DCM as solvent. After thorough drying, capsules were packed, and combusted using an Elementar Vario ISOTOPE EA (Elemental Analyzer), and the isotopic ratios (^{14}C/^{12}C) of produced CO$_2$ were determined via the directly connected AMS, the MICADAS system, which is equipped with a gas-ion source. Radiocarbon contents of the samples were analyzed along with reference standards (oxalic acid II; NIST SRM 4990 C) and blanks (phthalic anhydride; Sigma-Aldrich 320064)[110]. Background correction and standard normalization were performed via the BATS software. Corrections for the procedural blank were made using the approach described in Sun et al.[116]. Briefly, several aliquots of differently sized FAMEs were extracted from two in-house reference materials with known radiocarbon content, namely a modern apple peel with Fraction Modern relative to the reference standard (F^{14}C$_{OC}$) = 1.029 ± 0.001 and ^{14}C-free Eocene Messel shale with F^{14}C$_{OC}$ = 0, using the same procedures applied for the samples

studied here. Assuming constant blank contribution, mass and radiocarbon signature of the blank were determined, and F^{14}C values of unknown FAME samples were corrected for its contribution, with full propagation of uncertainties. An additional correction was implemented for the addition of the methyl group[15,116], since it affects the slope of the regression lines. In order to remove its contribution from the blank assessment, the F^{14}C values the unprocessed fatty acids would have if they were methylated have to be calculated. This was achieved by combining the F^{14}C of the bulk apple peel and the FAs with the F^{14}C$_{methyl}$ through isotopic mass balance[15].

Data availability

References

1. Denton, G. H. et al. The last glacial termination. *Science* **328**, 1652–1656 (2010).
2. Marcott, S. A. et al. Centennial-scale changes in the global carbon cycle during the last deglaciation. *Nature* **514**, 616–619 (2014).
3. Shakun, J. D. & Carlson, A. E. A global perspective on Last Glacial Maximum to Holocene climate change. *Quat. Sci. Rev.* **29**, 1801–1816 (2010).
4. Rasmussen, S. O. et al. A new Greenland ice core chronology for the last glacial termination. *J. Geophys. Res. Atmos.* **111**, D06102 (2006).
5. Brendryen, J., Haflidason, H., Yokoyama, Y., Haaga, K. A. & Hannisdal, B. Eurasian ice sheet collapse was a major source of Meltwater Pulse 1A 14,600 years ago. *Nat. Geosci.* **13**, 363–368 (2020).
6. Deschamps, P. et al. Ice-sheet collapse and sea-level rise at the Bølling warming 14,600 years ago. *Nature* **483**, 559–564 (2012).
7. Buizert, C. et al. Greenland temperature response to climate forcing during the last deglaciation. *Science (1979)* **345**, 1177–1180 (2014).
8. Obase, T. & Abe-Ouchi, A. Abrupt Bølling-Allerød warming simulated under gradual forcing of the last deglaciation. *Geophys. Res. Lett.* **46**, 11397–11405 (2019).
9. Barker, S. & Knorr, G. Millennial scale feedbacks determine the shape and rapidity of glacial termination. *Nat. Commun.* **12**, 2273 (2021).
10. Sun, Y. et al. Ice sheet decline and rising atmospheric CO2 control AMOC sensitivity to deglacial meltwater discharge. *Glob. Planet Change* **210**, 103755 (2022).
11. Weaver, A. J., Saenko, O. A., Clark, P. U. & Mitrovica, J. X. Meltwater pulse 1A from Antarctica as a trigger of the Bølling-Allerød warm interval. *Science (1979)* **299**, 1709–1713 (2003).
12. Sévellec, F., Fedorov, A. V. & Liu, W. Arctic sea-ice decline weakens the Atlantic Meridional overturning circulation. *Nat. Clim. Chang.* **7**, 604–610 (2017).
13. Schaefer, K., Lantuit, H., Romanovsky, V. E., Schuur, E. A. G. & Witt, R. The impact of the permafrost carbon feedback on global climate. *Environ. Res. Letters* **9**, 085003 (2014).
14. Vonk, J. E. et al. Activation of old carbon by erosion of coastal and subsea permafrost in Arctic Siberia. *Nature* **489**, 137–140 (2012).
15. Winterfeld, M. et al. Deglacial mobilization of pre-aged terrestrial carbon from degrading permafrost. *Nat. Commun.* **9**, 3666 (2018).
16. Schuur, E. A. G. et al. Vulnerability of permafrost carbon to climate change: implications for the global carbon cycle. *Bioscience* **58**, 701–714 (2008).
17. Strauss, J. et al. Circum-arctic map of the Yedoma Permafrost domain. *Front. Earth Sci.* **9**, 758360 (2021).
18. Turetsky, M. R. et al. Carbon release through abrupt permafrost thaw. *Nat. Geosci.* **13**, 138–143 (2020).
19. Lindgren, A., Hugelius, G. & Kuhry, P. Extensive loss of past permafrost carbon but a net accumulation into present-day soils. *Nature* **560**, 219–222 (2018).
20. Romanovskii, N. N. et al. Thermokarst and land-ocean interactions, Laptev Sea region, Russia. *Permafr. Periglac. Process.* **11**, 137–152 (2000).

21. Romanovskii, N. N., Hubberten, H. W., Gavrilov, A. V., Tumskoy, V. E. & Kholodov, A. L. Permafrost of the east Siberian Arctic shelf and coastal lowlands. *Quat. Sci. Rev.* **23**, 1359–1369 (2004).

22. Martens, J. et al. Remobilization of dormant carbon from Siberian-Arctic permafrost during three past warming events. *Sci. Adv.* **6**, eabb6546 (2020).

23. Schirrmeister, L. et al. Sedimentary characteristics and origin of the Late Pleistocene Ice Complex on north-east Siberian Arctic coastal lowlands and islands - A review. *Quat. Int.* **241**, 3–25 (2011).

24. Strauss, J. et al. Deep Yedoma permafrost: a synthesis of depositional characteristics and carbon vulnerability. *Earth Sci. Rev.* **172**, 75–86 (2017).

25. Köhler, P., Knorr, G. & Bard, E. Permafrost thawing as a possible source of abrupt carbon release at the onset of the Bølling/Allerød. *Nat. Commun.* **5**, 5520 (2014).

26. Ciais, P. et al. Large inert carbon pool in the terrestrial biosphere during the Last Glacial Maximum. *Nat. Geosci.* **5**, 74–79 (2012).

27. Lantuit, H. et al. The arctic coastal dynamics database: a new classification scheme and statistics on arctic permafrost coastlines. *Estuaries Coasts* **35**, 383–400 (2012).

28. Lantuit, H., Overduin, P. P. & Wetterich, S. Recent progress regarding permafrost coasts. *Permafr. Periglac. Process.* **24**, 120–130 (2013).

29. Schuur, E. A. G. et al. Climate change and the permafrost carbon feedback. *Nature* **520**, 171–179 (2015).

30. Chauhan, T., Noormets, R. & Rasmussen, T. L. Glaciomarine sedimentation and bottom current activity on the north-western and northern continental margins of Svalbard during the late Quaternary. *Geo-Marine Letters* **36**, 81–99 (2016).

31. Chauhan, T., Rasmussen, T. L. & Noormets, R. Palaeoceanography of the Barents Sea continental margin, north of Nordaustlandet, Svalbard, during the last 74 ka. *Boreas* **45**, 76–99 (2016).

32. Vogt, C. & Knies, J. Sediment dynamics in the Eurasian Arctic Ocean during the last deglaciation - The clay mineral group smectite perspective. *Mar. Geol.* **250**, 211–222 (2008).

33. Knies, J. & Stein, R. New aspects of organic carbon deposition and its paleoceanographic implications along the Northern Barents Sea Margin during the last 30,000 years. *Paleoceanography* **13**, 384–394 (1998).

34. Ramsey, C. B. Bayesian analysis of radiocarbon dates. *Radiocarbon* **51**, 337–360 (2009).

35. Heaton, T. J. et al. Marine20 - The Marine. *Radiocarb Age Calibration Curve (0-55,000 cal BP). Radiocarbon* **62**, 779–820 (2020).

36. Keigwin, L. D. et al. Deglacial floods in the Beaufort Sea preceded Younger Dryas cooling. *Nat. Geosci.* **11**, 599–604 (2018).

37. Matthiessen, J., Knies, J., Nowaczyk, N. R. & Stein, R. Late Quaternary dinoflagellate cyst stratigraphy at the Eurasian continental margin, Arctic Ocean: indications for Atlantic water inflow in the past 150,000 years. *Global Planet. Change* **31**, 65–86 (2001).

38. Goñi, M. A. & Hedges, J. I. Lignin dimers: structures, distribution, and potential geochemical applications. *Geochim. Cosmochim. Acta.* **56**, 4025–4043 (1992).

39. Tesi, T. et al. Composition and fate of terrigenous organic matter along the Arctic land-ocean continuum in East Siberia: insights from biomarkers and carbon isotopes. *Geochim. Cosmochim. Acta.* **133**, 235–256 (2014).

40. Vinšová, P. et al. The biogeochemical legacy of arctic subglacial sediments exposed by glacier retreat. *Global Biogeochem. Cycles* **36**, e2021GB007126 (2022).

41. Kim, D., Kim, J.-H., Jang, K. & Jung, J. Y. Large contributions of petrogenic and subglacial organic carbon to Arctic fjord sediments in Svalbard. https://doi.org/10.21203/rs.3.rs-2286733/v1 (2022).

42. Krajewska, M., Lubecki, L. & Szymczak-Żyła, M. Sources of sedimentary organic matter in Arctic fjords: evidence from lipid molecular markers. *Cont. Shelf Res.* **264**, 105053 (2023).

43. Dallmann, W. K. (Winfried K.). *Geoscience atlas of Svalbard.* (Norsk Polarinstitutt, 2015).

44. Tissot, B. P. & Welte, D. H. *Petroleum Formation and Occurrence.* (Springer Verky, 1984).

45. Petrini, M. et al. Simulated last deglaciation of the Barents Sea Ice Sheet primarily driven by oceanic conditions. *Quat. Sci. Rev.* **238**, 106314 (2020).

46. Hughes, A. L. C., Gyllencreutz, R., Lohne, Ø. S., Mangerud, J. & Svendsen, J. I. The last Eurasian ice sheets - a chronological database and time-slice reconstruction, DATED-1. *Boreas* **45**, 1–45 (2016).

47. Jessen, S. P., Rasmussen, T. L., Nielsen, T. & Solheim, A. A new Late Weichselian and Holocene marine chronology for the western Svalbard slope 30,000–0 cal years BP. *Quat. Sci. Rev.* **29**, 1301–1312 (2010).

48. le Heron, D. P. et al. An introduction to glaciated margins: the sedimentary and geophysical archive. in *Geological Society Special Publication* vol. 475 1–8 (Geological Society of London, 2019).

49. Bröder, L. et al. Fate of terrigenous organic matter across the Laptev Sea from the mouth of the Lena River to the deep sea of the Arctic interior. *Biogeosciences* **13**, 5003–5019 (2016).

50. Wahsner, M. et al. Clay-mineral distribution in surface sediments of the Eurasian Arctic Ocean and continental margin as indicator for source areas and transport pathways - a synthesis. *Boreas* **28**, 215–233 (1999).

51. Elverhøi, A. et al. The growth and decay of the late Weichselian ice sheet in Western svalbard and adjacent areas based on provenance studies of marine sediments. *Quat. Res.* **44**, 303–316 (1995).

52. Hogan, K. A. et al. Subglacial sediment pathways and deglacial chronology of the northern Barents Sea Ice Sheet. *Boreas* **46**, 750–771 (2017).

53. Kaiser, J., van der Meer, M. T. J. & Arz, H. W. Long-chain alkenones in Baltic Sea surface sediments: new insights. *Org. Geochem.* **112**, 93–104 (2017).

54. Brassell, S. C., Eglinton, G., Marlowe, I. T., Pflaumann, U. & Sarnthein, M. Molecular stratigraphy: a new tool for climatic assessment. *Nature* **320**, 129–133 (1986).

55. Weiss, G. M. et al. Alkenone Distributions and Hydrogen Isotope Ratios Show Changes in Haptophyte Species and Source Water in the Holocene Baltic Sea. *Geochem. Geophys. Geosys.* **21**, e2019GC00875 (2020).

56. Wang, K. J. et al. Group 2i Isochrysidales produce characteristic alkenones reflecting sea ice distribution. *Nat. Commun.* **12**, 15 (2021).

57. Liao, S., Wang, K. J. & Huang, Y. Unusually high production of C37:4 alkenone by an Arctic Gephyrocapsa huxleyi strain grown under nutrient-replete conditions. *Org. Geochem.* 104539 https://doi.org/10.1016/j.orggeochem.2022.104539 (2022).

58. Bendle, J., Rosell-Melé, A. & Ziveri, P. Variability of unusual distributions of alkenones in the surface waters of the Nordic seas. *Paleoceanography* **20**, 1–15 (2005).

59. Rosell-Melé, A., Jansen, E. & Weinelt, M. Appraisal of a molecular approach to infer variations in surface ocean freshwater inputs into the North Atlantic during the last glacial. *Glob. Planet Change* **34**, 143–152 (2002).

60. Zheng, Y., Heng, P., Conte, M. H., Vachula, R. S. & Huang, Y. Systematic chemotaxonomic profiling and novel paleotemperature indices based on alkenones and alkenoates: Potential for disentangling mixed species input. *Org. Geochem.* **128**, 26–41 (2019).

61. Belt, S. T. et al. A reproducible method for the extraction, identification and quantification of the Arctic sea ice proxy IP 25 from marine sediments. *Anal. Methods* **4**, 705–713 (2012).

62. Belt, S. T. & Müller, J. The Arctic sea ice biomarker IP25: a review of current understanding, recommendations for future research and applications in palaeo sea ice reconstructions. *Quat. Sci. Rev.* **79**, 9–25 (2013).

63. Belt, S. T., Smik, L., Köseoğlu, D., Knies, J. & Husum, K. A novel biomarker-based proxy for the spring phytoplankton bloom in Arctic and sub-arctic settings – HBI T25. *Earth Planet Sci. Lett.* **523**, 115703 (2019).

64. Volkman, J. K. A review of sterol markers for marine and terrigenous organic matter. *Org. Geochem.* **9**, 83–99 (1986).

65. Müller, J., Massé, G., Stein, R. & Belt, S. T. Variability of sea-ice conditions in the Fram Strait over the past 30,000 years. *Nat. Geosci.* **2**, 772–776 (2009).

66. Xiao, X., Stein, R. & Fahl, K. MIS 3 to MIS 1 temporal and LGM spatial variability in Arctic Ocean sea ice cover: Reconstruction from biomarkers. *Paleoceanography* **30**, 969–983 (2015).

67. Meyer, V. D. et al. Permafrost-carbon mobilization in Beringia caused by deglacial meltwater runoff, sea-level rise and warming. *Environ. Res. Lett.* **14**, 085003 (2019).

68. Feng, X. et al. Differential mobilization of terrestrial carbon pools in Eurasian Arctic river basins. *Proc. Natl Acad. Sci. USA.* **110**, 14168–14173 (2013).

69. Martens, J. et al. CASCADE-The Circum-Arctic Sediment CArbon DatabasE. *Earth Syst. Sci. Data* **13**, 2561–2572 (2021).

70. Jónsdóttir, I. S. Terrestrial ecosystems on Svalbard: heterogeneity, complexity and fragility from an Arctic island perspective. *Biol. Environ.: Proc. Royal Irish Acad.* **105**, 155–165 (2005).

71. Johansen, B. E., Karlsen, S. R. & Tømmervik, H. Vegetation mapping of Svalbard utilising Landsat TM/ETM+ data. *Polar Record* **48**, 47–63 (2012).

72. Eglinton, G. & Hamilton, R. J. The Distribution of Alkanes. in *Chemical Plant Taxonomy* (ed. Swain, T.) vol. 8 187–217 (Academic Press, 1963).

73. Fransner, O., Noormets, R., Flink, A. E., Hogan, K. A. & Dowdeswell, J. A. Sedimentary processes on the continental slope off Kvitøya and Albertini troughs north of Nordaustlandet, Svalbard – The importance of structural-geological setting in trough-mouth fan development. *Mar. Geol.* **402**, 194–208 (2018).

74. Bröder, L., Tesi, T., Andersson, A., Semiletov, I. & Gustafsson, Ö. Bounding cross-shelf transport time and degradation in Siberian-Arctic land-ocean carbon transfer. *Nat. Commun.* **9**, 806 (2018).

75. Patton, H. et al. Deglaciation of the Eurasian ice sheet complex. *Quat. Sci. Rev.* **169**, 148–172 (2017).

76. Ingólfsson, Ó. & Landvik, J. Y. The Svalbard-Barents Sea ice-sheet-Historical, current and future perspectives. *Quat. Sci. Rev.* **64**, 33–60 (2013).

77. Svendsen, J. I. et al. Late Quaternary ice sheet history of northern Eurasia. *Quat. Sci. Rev.* **23**, 1229–1271 (2004).

78. Shackleton, C. et al. Subglacial water storage and drainage beneath the Fennoscandian and Barents Sea ice sheets. *Quat. Sci. Rev.* **201**, 13–28 (2018).

79. Shackleton, C. et al. Distinct modes of meltwater drainage and landform development beneath the last Barents Sea ice sheet. *Front. Earth Sci. (Lausanne)* **11**, 1111396 (2023).

80. Hebbeln, D. & Wefer, G. Effects of ice coverage and ice-rafted material on sedimentation in the Fram Strait. *Nature* **350**, 409–411 (1991).

81. Stein, R. et al. The last deglaciation event in the Eastern Central Arctic Ocean. *Science (1979)* **264**, 692–696 (1994).

82. Krumpen, T. et al. Variability and trends in Laptev Sea ice outflow between 1992-2011. *Cryosphere* **7**, 349–363 (2013).

83. Wegner, C. et al. Sediment entrainment into sea ice and transport in the Transpolar Drift: a case study from the Laptev Sea in winter 2011/2012. *Cont. Shelf Res.* **141**, 1–10 (2017).

84. Lindemann, F., Hölemann, J. A., Korablev, A. & Zachek, A. Particle Entrainment into Newly Forming Sea Ice—Freeze-Up Studies in October 1995. in *Land-Ocean Systems in the Siberian Arctic* 113–123 https://doi.org/10.1007/978-3-642-60134-7_12 (Springer Berlin Heidelberg, 1999).

85. Nürnberg, D. et al. Sediments in Arctic sea ice: Implications for entrainment, transport and release. *Mar. Geol.* **119**, 185–214 (1994).

86. Dethleff, D. & Kuhlmann, G. Fram Strait sea-ice sediment provinces based on silt and clay compositions identify Siberian Kara and Laptev seas as main source regions. *Polar Res.* **29**, 265–282 (2010).

87. Stierle, A. P. & Eicken, H. Sediment inclusions in Alaskan Coastal Sea Ice: spatial distribution, interannual variability, and entrainment requirements. *Arct. Antarct. Alp. Res.* **34**, 465–476 (2002).

88. Reimnitz, E., Barnes, P. W. & Weber, W. S. Particulate matter in pack ice of the Beaufort Gyre. *J. Glaciol.* **39**, 186–198 (1993).

89. Pfirman, S. L., Colony, R., Nürnberg, D., Eicken, H. & Rigor, I. Reconstructing the origin and trajectory of drifting Arctic sea ice. *J. Geophys. Res. Oceans* **102**, 12575–12586 (1997).

90. Tovar-Sánchez, A. et al. Impacts of metals and nutrients released from melting multiyear Arctic sea ice. *J. Geophys. Res.* **115**, C07003 (2010).

91. Meiners, K. M. & Michel, C. Dynamics of nutrients, dissolved organic matter and exopolymers in sea ice. in *Sea Ice* 415–432 https://doi.org/10.1002/9781118778371.ch17 (John Wiley & Sons, Ltd, 2016).

92. Müller, J. & Stein, R. High-resolution record of late glacial and deglacial sea ice changes in Fram Strait corroborates ice-ocean interactions during abrupt climate shifts. *Earth Planet Sci. Lett.* **403**, 446–455 (2014).

93. Stein, R., Fahl, K. & Müller, J. Proxy reconstruction of Cenozoic Arctic Ocean Sea-Ice History – from IRD to IP25. *Polarforschung* **82**, 37–71 (2012).

94. Spreen, G. et al. Arctic sea ice volume export through fram strait from 1992 to 2014. *J. Geophys. Res. Oceans* **125**, e2019JC016039 (2020).

95. Smedsrud, L. H., Halvorsen, M. H., Stroeve, J. C., Zhang, R. & Kloster, K. Fram Strait sea ice export variability and September Arctic sea ice extent over the last 80 years. *Cryosphere* **11**, 65–79 (2017).

96. Idier, D., Paris, F., Cozannet, Gle, Boulahya, F. & Dumas, F. Sea-level rise impacts on the tides of the European Shelf. *Cont. Shelf Res.* **137**, 56–71 (2017).

97. Egbert, G. D., Ray, R. D. & Bills, B. G. Numerical modeling of the global semidiurnal tide in the present day and in the last glacial maximum. *J. Geophys. Res. Oceans* **109**, C03003 (2004).

98. Uehara, K., Scourse, J. D., Horsburgh, K. J., Lambeck, K. & Purcell, A. P. Tidal evolution of the northwest European shelf seas from the Last Glacial Maximum to the present. *J. Geophys. Res. Oceans* **111**, C09025 (2006).

99. Schirrmeister, L. et al. The genesis of Yedoma Ice Complex permafrost – grain-size endmember modeling analysis from Siberia and Alaska. *E&G Quat. Sci.* **69**, 33–53 (2020).

100. Schirrmeister, L. et al. Yedoma ice complex of the Buor Khaya Peninsula (southern Laptev Sea). *Biogeosciences* **14**, 1261–1283 (2017).

101. Winterfeld, M., Goñi, M. A., Just, J., Hefter, J. & Mollenhauer, G. Characterization of particulate organic matter in the Lena River delta and adjacent nearshore zone, NE Siberia – Part 2: Lignin-derived phenol compositions. *Biogeosciences* **12**, 2261–2283 (2015).

102. Lambeck, K., Rouby, H., Purcell, A., Sun, Y. & Sambridge, M. Sea level and global ice volumes from the Last Glacial Maximum to the Holocene. *Proc. Natl Acad. Sci. USA* **111**, 15296–15303 (2014).

103. Ślubowska, M. A., Koç, N., Rasmussen, T. L. & Klitgaard-Kristensen, D. Changes in the flow of Atlantic water into the Arctic Ocean since the last deglaciation: Evidence from the northern Svalbard continental margin, 80°N. *Paleoceanography* **20**, PA4014 (2005).

104. Stroeve, J. C. et al. The Arctic's rapidly shrinking sea ice cover: a research synthesis. *Clim. Change* **110**, 1005–1027 (2012).

105. Smedsrud, L. H. et al. Nordic Seas Heat Loss, Atlantic Inflow, and Arctic Sea Ice Cover Over the Last Century. *Rev. Geophys.* **60**, e2020RG000725 (2022).

106. Tesi, T. et al. Massive remobilization of permafrost carbon during post-glacial warming. *Nat. Commun.* **7**, 13653 (2016).

107. Martens, J. et al. Remobilization of old permafrost carbon to chukchi sea sediments during the end of the last deglaciation. *Global Biogeochem. Cycles* **33**, 2–14 (2019).

108. Günther, F. et al. Observing Muostakh disappear: permafrost thaw subsidence and erosion of a ground-ice-rich island in response to arctic summer warming and sea ice reduction. *Cryosphere* **9**, 151–178 (2015).

109. Irrgang, A. M. et al. Variability in rates of coastal change along the Yukon Coast, 1951 to 2015. *J. Geophys. Res. Earth Surf.* **123**, 779–800 (2018).

110. Mollenhauer, G., Grotheer, H., Gentz, T., Bonk, E. & Hefter, J. Standard operation procedures and performance of the MICADAS radiocarbon laboratory at Alfred Wegener Institute (AWI), Germany. *Nucl. Instrum. Methods Phys. Res. B.* **496**, 45–51 (2021).

111. Tesi, T. et al. Resolving sea ice dynamics in the north-western Ross Sea during the last 2.6 ka: from seasonal to millennial timescales. *Quat. Sci. Rev.* **237**, 106299 (2020).

112. Goñi, M. A. & Montgomery, S. Alkaline CuO oxidation with a microwave digestion system: Lignin analyses of geochemical samples. *Anal. Chem.* **72**, 3116–3121 (2000).

113. Tesi, T. et al. Rapid Atlantification along the Fram Strait at the beginning of the 20th century. *Sci. Adv.* **7**, 2946 (2021).

114. Rontani, J. F., Wakeham, S. G., Prahl, F. G., Vaultier, F. & Volkman, J. K. Analysis of trace amounts of alkenones in complex environmental samples by way of NaBH4/NaBD4 reduction and silylation. *Org. Geochem.* **42**, 1299–1307 (2011).

115. Eglinton, T. I., Aluwihare, L. I., Bauer, J. E., Druffel, E. R. M. & Mcnichol, A. P. Gas chromatographic isolation of individual compounds from complex matrices for radiocarbon dating. *Anal. Chem.* **68**, 904–912 (1996).

116. Sun, S. et al. 14C blank assessment in small-scale compound-specific radiocarbon analysis of lipid biomarkers and lignin phenols. *Radiocarbon* **62**, 207–218 (2020).

117. Jakobsson, M. et al. The International Bathymetric Chart of the Arctic Ocean Version 4.0. *Sci. Data* **7**, (2020).

118. Dyke, A. S., Moore, A. J. & Robertson, L. Deglaciation of North America. *Geolog. Survey Can, Open File 1574* (2003).

119. North Greenland Ice Core Project members. High-resolution record of Northern Hemisphere climate extending into the last interglacial period. *Nature* **431**, 147–151 (2004).

Acknowledgements

Author contributions

A.N. and T.T. planned the research project and activities. R.N. and T.C. provided the sediment and foraminifera samples. F.M. developed the age-depth model. L.C. and C.P. helped with the radiocarbon dating on foraminifera. A.N. carried out the biogeochemical analysis of all samples. H.G. and J.H. carried out the analysis and quantification of CSRA. A.N. drafted the figures. A.N., T.T., S.B., G.M. and F.C. interpreted the data. All authors contributed to the final manuscript.

Competing interests

The authors declare no competing interests.

Additional information

Supplementary information The online version contains supplementary material available at https://doi.org/10.1038/s43247-023-01013-y.

Correspondence and requests for materials should be addressed to Alessio Nogarotto.

Peer review information *Communications Earth and Environment* thanks Henry Patton and the other, anonymous, reviewer for their contribution to the peer review of this work. Primary Handling Editors: Rachael Rhodes, Aliénor Lavergne and Joe Aslin. A peer review file is available.

Reprints and permission information is available at http://www.nature.com/reprints